

1 **Implications of laterally varying scattering properties**
2 **for subsurface monitoring with coda wave sensitivity**
3 **kernels: application to volcanic and fault zone setting**

4 **Chantal van Dinther**¹, **Ludovic Margerin**², **Michel Campillo**¹

5 ¹Université Grenoble Alpes, ISTerre, C.N.R.S., B.P. 53, 38041 Grenoble, France.

6 ²Institut de Recherche en Astrophysique et Planétologie, Université Toulouse III Paul Sabatier, C.N.R.S.,

7 C.N.E.S, 14, Av. Edouard Belin, 31400 Toulouse, France.

8 **Key Points:**

- 9 • A non-uniform distribution of scattering strength can have a profound impact on
10 the spatio-temporal sensitivity of coda waves.
- 11 • We illustrate this using Monte Carlo simulations for models with either a volcanic,
12 fault zone or two half-spaces setting.
- 13 • The mean intensity, specific intensity and energy flux, is key to understanding the
14 decorrelation, travel-time and intensity kernels, respectively.

Corresponding author: Chantal van Dinther, chantal.van-dinther@univ-grenoble-alpes.fr

Abstract

Monitoring changes of seismic properties at depth can provide a first order insight into Earth's dynamic evolution. Coda wave interferometry is the primary tool for this purpose. This technique exploits small changes of waveforms in the seismic coda and relates them to temporal variations of attenuation or velocity at depth. While most existing studies assume statistically homogeneous scattering strength in the lithosphere, geological observations suggest that this hypothesis may not be fulfilled in active tectonic or volcanic areas. In a numerical study we explore the impact of a non-uniform distribution of scattering strength on the spatio-temporal sensitivity of coda waves. Based on Monte Carlo simulation of the radiative transfer process, we calculate sensitivity kernels for three different observables, namely travel-time, decorrelation and intensity. Our results demonstrate that laterally varying scattering properties can have a profound impact on the sensitivities of coda waves. Furthermore, we demonstrate that the knowledge of the mean intensity, specific intensity and energy flux, governed by spatial variation of scattering strength, is key to understanding the decorrelation, travel-time and intensity kernels, respectively. A number of previous works on coda wave sensitivity kernels neglect the directivity of energy fluxes by employing formulas extrapolated from the diffusion approximation. In this work, we demonstrate and visually illustrate the importance of the use of specific intensity for the travel-time and scattering kernels, in the context of volcanic and fault zone setting models. Our results let us foresee new applications of coda wave monitoring in environments of high scattering contrast.

Plain Language Summary

To monitor the evolution of the dynamic Earth, seismologists use a part of the seismic record called 'coda', which is composed of waves that have bounced multiple times off heterogeneities of the crust. The coda is extremely sensitive to weak perturbations of propagation properties induced by Earth's tectonic and volcanic activity. The correct physical modeling of coda waves is therefore key to unravel the rich information encoded in their waveforms. A limitation of current seismological monitoring techniques is the neglect of strong lateral variations of coda waves propagation properties documented by geological observations. Our work focuses specifically on this aspect. We provide a complete theoretical and numerical framework to model and understand the spatial and temporal sensitivity of coda waves to medium perturbations in complex geological settings.

47 Using simple but realistic models of a fault zone and a volcano, we illustrate the profound
48 impact of non-uniform scattering properties on the coda wave sensitivity, which in turn
49 determines the ability of seismologists to correctly retrieve the magnitude and location
50 of physical changes in the crust. Our results let us foresee new applications of coda wave
51 monitoring in environments of high scattering contrast, such as volcanic and fault zone
52 settings.

53 **1 Introduction**

54 With the recent advancements in seismic sensor techniques and the rapid deploy-
55 ment of (dense) seismic arrays over the last decade, there has been a surge in the num-
56 ber of monitoring studies aiming to capture the dynamic evolution of the subsurface. Due
57 to scattering, coda waves sample a large volume of the subsurface densely for long prop-
58 agation times and are thus sensitive to weak changes of the medium. Consequently, coda
59 waves may be more suitable to characterise temporal variations of the Earth's crust than
60 direct waves, which only sample a narrow volume along the ray path between the (vir-
61 tual) source and detector. Poupinet et al. (1984) were first to demonstrate the feasibil-
62 ity of monitoring weak changes in apparent velocity caused by fault activity in Califor-
63 nia using coda waves. Poupinet et al. (1984) derived these global medium changes by
64 measuring the phase shift between the coda of earthquake doublets. In numerical and
65 lab experiments, the extreme sensitivity of the seismic coda to temporal medium changes
66 has also been demonstrated by Snieder et al. (2002). Later, detection of temporal medium
67 changes has been successfully applied using the coda of earthquake records or the coda
68 of ambient noise cross-correlations in numerous settings including but not limited to: vol-
69 canoes (e.g. Sens-Schönfelder & Wegler, 2006; Mordret et al., 2010; Brenguier et al., 2016;
70 Hirose et al., 2017; Sánchez-Pastor et al., 2018; Mao et al., 2019; Obermann, Planes, et
71 al., 2013), fault zones (e.g. Schaff & Beroza, 2004; Peng & Ben-Zion, 2006; Wu et al.,
72 2009; Roux & Ben-Zion, 2014; Rivet et al., 2014; Brenguier et al., 2008; Chen et al., 2010),
73 and CO₂ and geothermal reservoirs (Hillers et al., 2020, 2015; Obermann et al., 2015).

74 Although measurements of temporal medium changes are interesting in their own
75 right, knowledge about their spatial location is necessary to gain more insight into the
76 processes that occur at depth. Regionalization of data can yield a first order estimate
77 on the spatial distribution, but a preferable approach is to perform a (linear) inversion
78 using so-called sensitivity kernels. In loose terms, these spatial weighting functions pro-

79 vide information on the parts of the medium that have preferentially been sampled by
80 the waves in a probabilistic sense. The first travel-time sensitivity kernels for coda wave
81 interferometry have been introduced by Pacheco and Snieder (2005) under the diffusion
82 approximation. Shortly after, Pacheco and Snieder (2006) provided probabilistic kernels
83 for the single scattering regime. Both kernels are in the form of a spatio-temporal con-
84 volution of mean intensities of the coda waves. Obermann, Planes, et al. (2013) applied
85 those kernels to invert for structural and temporal velocity changes around the Piton de
86 la Fournaise volcano on Reunion Island. To detect and locate medium changes caused
87 by the M_w 7.9, 2008 earthquake in Wenchuan in China, Obermann et al. (2019) used
88 a 3-D kernel combining the sensitivity of body and surface waves. Although the results
89 of the authors were very promising, Margerin et al. (2016) raised questions about the
90 formulas used to compute the sensitivity kernels, since the works rely on an extrapola-
91 tion of a formula established in the diffusion regime. Margerin et al. (2016) demonstrated
92 that knowledge of the angular distribution of the energy fluxes of coda waves is required
93 for an accurate prediction of sensitivities, valid for an arbitrary distribution of hetero-
94 geneities and all propagation regimes. The authors obtained this result by using a ra-
95 diative transfer approach, which directly predicts specific intensities. Other developments
96 on sensitivity kernels focus on the sensitivity as a function of depth. Obermann et al.
97 (2016); Obermann, Planès, et al. (2013) showed that a linear combination of the 2-D sur-
98 face wave and 3-D body wave kernels are a decent proxy to describe the sensitivity as
99 function of lapse-time and depth. A formal approach to couple body and surface waves
100 is provided by Margerin et al. (2019), leading to a specific formulation of kernels (Barajas,
101 2021).

102 Most of these studies on sensitivity kernels provide a solution for statistically ho-
103 mogeneous scattering media, although the interest in extending the sensitivity kernels
104 to non-uniform media is growing, which is especially interesting for monitoring volcanic
105 and fault zone settings. Wegler and Lühr (2001) derived attenuation parameters around
106 the Merapi volcano in Indonesia. The authors found a scattering mean free path (ℓ) as
107 low as 100 m for S waves in the frequency band of 4-20 Hz. They also reported that the
108 scattering attenuation is at least one order of magnitude larger than the intrinsic atten-
109 uation around Merapi. Later, Yoshimoto et al. (2006) estimated scattering attenuation
110 in the north-eastern part of Honshu in Japan. For this volcanic area the authors anal-
111 ysed the coda of earthquake records and reported a scattering coefficient of 0.01 km^{-1}

112 for the frequency of 10 Hz. Another study that analysed the coda of seismograms in a
 113 volcanic setting in Japan found the scattering mean free path for P and S waves to be
 114 as short as 1 km for the 8-16 Hz frequency band (Yamamoto & Sato, 2010). Recently,
 115 Hirose et al. (2019) derived a scattering mean free path ~ 2 km at Sakurajima volcano
 116 in Japan, which is much smaller than in the surrounding rock. In a recent study on the
 117 western part of the North Anatolian Fault Zone (NAFZ) van Dinther et al. (2020) also
 118 found a strong contrast in scattering (\sim factor of 15), with $\ell = 10$ km inside the fault
 119 zone and ℓ in the order of 150 km outside the fault zone. Gaebler et al. (2019) found sim-
 120 ilarly small scattering mean free path values along the northern strand of the NAFZ analysing
 121 the energy decay of earthquake records with a central frequency of 0.75 Hz.

122 The first works considering non-uniform media are by Kanu and Snieder (2015a)
 123 and Kanu and Snieder (2015b) in which the authors use ensemble averaging of the coda
 124 envelopes modelled by employing the diffusion equation to numerically compute the decor-
 125 relation sensitivity kernels, which are interpreted as travel-time kernels, to image veloc-
 126 ity variations in 2-D acoustic heterogeneous media. Snieder et al. (2019) adjusted the
 127 approach to (1) a 2-D elastic case based on the diffusion equation and (2) a 2-D acous-
 128 tic case based on radiative transfer theory, for media with weak velocity variations. Build-
 129 ing on the work of Snieder et al. (2019) and assuming diffusive wave propagation, Duran
 130 et al. (2020) developed a numerical approach to derive elastic and acoustic decorrelation
 131 sensitivity kernels for 2-D heterogeneous scattering media. Recently, Zhang et al. (2021)
 132 modeled sensitivity kernels for elastic body waves in 2-D random heterogeneous scatter-
 133 ing media based on radiative transfer theory using a Monte Carlo approach. The authors
 134 use a similar probabilistic approach as is used in current study, but a different compu-
 135 tation method. Furthermore, the scattering contrasts considered in current study are larger.

136 In this work we explore the impact of scattering distribution on coda wave sensi-
 137 tivity kernels for the acoustic scalar case. The parametric part of this study (Section 4.2)
 138 aids in the understanding of the kernels. Finally, we show examples of sensitivity ker-
 139 nels for realistic settings.

140 **2 Coda-wave Sensitivity Kernels**

141 When monitoring the subsurface, one aims to invert observations to gain informa-
 142 tion about the perturbation of medium properties. As the name suggests, the sensitiv-

143 ity kernels quantify the spatial and temporal sensitivity of a specific observable to changes
 144 in the medium. The kernels facilitate the reconstruction in 2-D or 3-D of the spatial vari-
 145 ation of a given physical parameter, such as the wave speed or scattering properties. Since
 146 different observations require the use of different kernels, we compute three types of sen-
 147 sitivity kernels: the travel time kernel K_{tt} , the scattering kernel K_{sc} and the decorre-
 148 lation kernel K_{dc} .

149 The travel-time kernel, K_{tt} , relates the observed travel-time delay (or phase shifts)
 150 between data for different recording periods, which can be seen as apparent velocity changes,
 151 to the macroscopic true changes in elastic medium properties. In this study we use the
 152 kernel as defined by Margerin et al. (2016); Mayor et al. (2014):

$$K_{tt}(\mathbf{r}', t; \mathbf{r}, \mathbf{r}_0) = S^D \int_0^t \int_{S^D} \frac{I(\mathbf{r}', t - t', -\mathbf{n}'; \mathbf{r}) I(\mathbf{r}', t', \mathbf{n}'; \mathbf{r}_0) dt' dn'}{I(\mathbf{r}, t; \mathbf{r}_0)} \quad (1)$$

153 where S^D denotes the unit sphere in space dimension D , as well as its area. The
 154 intensity propagators I , for the intensities traveling from a source of forward intensity
 155 (\mathbf{r} ; in applications this can be seen as the ‘source’) to a source of backward intensity (\mathbf{r}_0 ;
 156 ‘detector’), via a perturbation (\mathbf{r}'), are based on the 2-D radiative transfer equation (RTE;
 157 Sato (1993); Paasschens (1997)). I will be presented in greater details later in this manuscript
 158 (see Section 4.1 for the description of the source of forward and backward intensity).

159 Note that the intensity, or energy density, has dimension $[L]^{-D}$ (Paasschens, 1997)
 160 so that the kernel has dimension $[t][L]^{-D}$. The kernels are a time density, such that they
 161 are equal to the time spent by the waves around a given point, per unit volume or sur-
 162 face. The numerator of Eq. (1) is a convolution between *specific* intensities of two sources,
 163 one source of forward intensity and one of backward intensity. A specific intensity is de-
 164 fined as the amount of energy flowing around direction \mathbf{n}' , through a small surface el-
 165 ement dS located at point \mathbf{r} and at a certain time t within a defined frequency band (e.g.
 166 Margerin, 2005). The validity of the kernels also holds for anisotropic scattering, although
 167 we consider only isotropic scattering in current work. Previously, Mayor et al. (2014) in-
 168 troduced a sensitivity kernel for the perturbation of intensity caused by a local change
 169 in absorption. In Margerin et al. (2016) this sensitivity kernel is reinterpreted probabilis-
 170 tically as the travel-time kernel.

A structural change in the subsurface, e.g. the growth of a fault, results in a perturbation of scattering. An extra scatterer creates new propagation paths for the waves, which in turn slightly modifies the coda signal. As a consequence, one can observe a decorrelation of the waveform in the recordings for different periods of time (Planès et al., 2014). The decorrelation kernel, K_{dc} , relates this observation to the change in scattering of the medium. The kernel takes into account the new propagation paths that have been created by the addition of scatterers, and is defined as follows (Planès et al., 2014; Margerin et al., 2016):

$$K_{dc}(\mathbf{r}', t; \mathbf{r}, \mathbf{r}_0) = \int_0^t \frac{I(\mathbf{r}', t - t'; \mathbf{r}) I(\mathbf{r}, t'; \mathbf{r}_0) dt'}{I(\mathbf{r}, t; \mathbf{r}_0)} \quad (2)$$

The intensities in Eq. (2) are *mean* intensities, therefore the decorrelation kernel is dependent on the mean energy densities only and not on the directivity of the intensities. Note that formula (2) is valid *stricto sensu* in the case where the structural change behaves as isotropic scatterers. In the scalar approximation employed in this work, this implies that they are small compared to the probing wavelength. We emphasize that the scattering properties of the reference medium may be completely arbitrary. Another observation for the same medium change, i.e. the scattering perturbation, is a change in intensity δI . Since the observation is different than in the case of the decorrelation, one needs another sensitivity kernel. Physically, a perturbation in scattering located in a volume $dV(\mathbf{r}')$ has two effects on the intensity. (1) An energy loss, which can be quantified by evaluating the extra-attenuation of seismic phonons that cross $dV(\mathbf{r}')$. This is effectively what can be monitored with K_{tt} . (2) An increased probability of energy reaching the detector due to the additional paths created by the additional scatterer. This is effectively what K_{dc} provides us with. Therefore, the scattering sensitivity kernel K_{sc} , as derived by Mayor et al. (2014), is defined as:

$$K_{sc}(\mathbf{r}', t; \mathbf{r}, \mathbf{r}_0) = K_{dc}(\mathbf{r}', t; \mathbf{r}, \mathbf{r}_0) - K_{tt}(\mathbf{r}', t; \mathbf{r}, \mathbf{r}_0) \quad (3)$$

171 Note that the scattering pattern of the new scatterers should be isotropic implying as
 172 above that they are small compared to the wavelength. A characteristic of this kernel
 173 is that the integral over all detection points \mathbf{r} gives 0, implied by the conservation of en-
 174 ergy as demonstrated in the work of Mayor et al. (2014). We will also find in the results
 175 (e.g. Fig. 2) that the scattering kernels have both positive and negative sensitivities to
 176 scattering perturbations. In other words, the spatial distribution of intensities is mod-

177 ified while the total intensities remain unchanged. For an extension of formulas (1), (2)
 178 and (3) to coupled P and S waves, the reader is referred to Zhang et al. (2021).

179 **3 Calculation of Sensitivity Kernels: a Monte Carlo Simulation Ap-** 180 **proach**

181 To compute the above defined sensitivity kernels we perform Monte Carlo simu-
 182 lations based on the 2-D RTE with isotropic scattering. This section is rather techni-
 183 cal in nature and may be read independently from the rest of the manuscript. We re-
 184 call that in a Monte Carlo approach (e.g. Margerin et al., 2000), the transport of energy
 185 is represented by random walks of discrete seismic “phonons” (Shearer & Earle, 2004)
 186 that undergo a sequence of collisions in a scattering and absorbing medium. In practice,
 187 the medium is often discretized onto elementary volumes where the number of phonons
 188 is monitored as a function of time to estimate the energy density. But it is also possi-
 189 ble to compute the energy density detected at a specific point of the medium by eval-
 190 uating the probability for the phonon to return to the detector at each scattering event
 191 (see e.g. Hoshiya, 1991, for a detailed treatment). In the present work, we adopt the lat-
 192 ter approach.

193 While early applications focused mostly on the computation of energy envelopes,
 194 the introduction of sensitivity kernels based on RTE has stimulated the development of
 195 Monte Carlo approaches to compute the derivatives of seismogram envelopes with re-
 196 spect to attenuation model parameters. In a recent investigation of PKP precursors, Sens-
 197 Schönfelder et al. (2020) use Monte Carlo simulations to compute the forward and back-
 198 ward intensities propagating from the source to the perturbation and from the detector
 199 to the perturbation, respectively. The convolution integral in Eq. (2)-(3) is then eval-
 200 uated numerically. The method highlights very nicely the regions of the deep Earth con-
 201 tributing to the detection of precursors. Recently, Zhang et al. (2021) generalized the
 202 radiative transfer formulation of sensitivities to the case of elastic body waves. These
 203 authors illustrate numerically the impact of non-uniform attenuation properties on the
 204 spatio-temporal dependence of the kernels in 2-D elastic media. The numerical approach
 205 is similar to Sens-Schönfelder et al. (2020) that relies on the convolution of forward and
 206 backward (specific) intensities evaluated by the Monte Carlo method. In this work, we
 207 propose yet another computational approach to the computation of kernels in non-uniform
 208 scattering media that exploits the idea of differential Monte Carlo simulations.

209 Takeuchi (2016) introduced a differential Monte Carlo method where both the en-
 210 velope and its partial derivative are calculated in a single simulation. An interesting ap-
 211 plication of the method, highlighting both the lateral and depth dependence of atten-
 212 uation in Japan, has been provided by Ogiso (2019). In this work, we also employ the
 213 differential approach but in a way quite distinct from Takeuchi (2016). For clarity, we
 214 recall the basic ingredients of the method in the next section.

215 3.1 Differential Monte Carlo Approach

The central idea of the differential Monte Carlo method is best explained with an
 example (see Lux & Koblinger, 1991, for a detailed treatment). Consider for instance
 the impact of a perturbation of the scattering coefficient on the energy density. Suppose
 that a seismic phonon has just been scattered at point \mathbf{r}' in a reference medium with scat-
 tering coefficient g . The probability density function (pdf) of the position \mathbf{r} of the next
 collision point may be written as:

$$P(\mathbf{r}; \mathbf{r}' | g) = g(\mathbf{r}) e^{-\int_{\mathbf{r}'}^{\mathbf{r}} g(\mathbf{x}) dx} \quad (4)$$

216 where the integral is carried on the ray connecting the point \mathbf{r}' to the point \mathbf{r} . Note that
 217 we allow the scattering coefficient to vary spatially in the reference medium. The dis-
 218 tribution of path length in the perturbed medium is obtained by the substitution $g \rightarrow$
 219 $g + \delta g$ in Eq. (4). In the differential Monte Carlo method, the envelopes in the refer-
 220 ence and perturbed medium are calculated simultaneously via a biasing scheme for the
 221 latter (Lux & Koblinger, 1991). To picture the idea, one may imagine a “true” phonon
 222 propagating in the reference medium and a “virtual” mate following *exactly* the same
 223 trajectory as the “true” phonon albeit in the perturbed medium. As the phonon prop-
 224 agates in the reference medium, the statistical weight of its virtual mate is updated to
 225 compensate exactly for the genuine frequency of occurrence of the path in the perturbed
 226 medium. As an example, let us consider the change of weight occurring after the phonon
 227 has left the collision point \mathbf{r}' until it is scattered again at point \mathbf{r} . Denoting by w the cor-
 228 rection factor, we find:

$$\begin{aligned}
w(\mathbf{r}; \mathbf{r}') &= \frac{P(\mathbf{r}; \mathbf{r}' | g + \delta g)}{P(\mathbf{r}; \mathbf{r}' | g)} \\
&= \frac{(g(\mathbf{r}) + \delta g(\mathbf{r})) e^{-\int_{\mathbf{r}'}^{\mathbf{r}} \delta g(\mathbf{x}) dx}}{g(\mathbf{r})}
\end{aligned}$$

An obvious condition of applicability is that $g(\mathbf{r}) > 0$, implying that a collision is indeed possible at the point \mathbf{r} in the reference medium. We also remark that there is no assumption on the 'smallness' of δg in the derivation of (5). For the computation of sensitivity kernels, we thus further require $\delta g/g \ll 1$ and perform a Taylor expansion to obtain (Takeuchi, 2016; Ogiso, 2019):

$$w(\mathbf{r}; \mathbf{r}') = 1 + \frac{\delta g(\mathbf{r})}{g(\mathbf{r})} - \int_{\mathbf{r}'}^{\mathbf{r}} \delta g(\mathbf{x}) dx \quad (5)$$

229 The interpretation of the above formula is as follows: as the virtual phonon propagates
230 between the two collision points \mathbf{r}' and \mathbf{r} , its weight decreases progressively following the
231 integral term; at the collision point \mathbf{r} , its weight undergoes a positive jump $\delta g(\mathbf{r})/g(\mathbf{r})$.
232 These two contributions may respectively be related to the loss and gain terms in Eq.
233 (3).

234 There are two difficulties in the practical application of formula (5). The first one
235 becomes apparent when one discretizes the kernel onto a grid of pixels (in 2-D, or vox-
236 els in 3-D): the path of the particle inside each pixel has to be carefully monitored to cal-
237 culate the integral in Eq. (5). Such particle tracking can be at the origin of significant
238 computational overhead. The other difficulty is inherent to the spatial variation of the
239 scattering coefficient. Generating the exact path length distribution for the pdf (4) in-
240 volves the computation of the line integral of g which may be very time consuming. In
241 what follows, we propose a method that solves both of these issues by transferring all
242 the sensitivity computation to collision points. A strength of the method is that parti-
243 cle tracking is minimal. Furthermore, a completely arbitrary distribution of scattering
244 properties -including discontinuities of the scattering coefficient- may be implemented
245 transparently and in an "exact" fashion. The main drawback of the approach is that the
246 introduction of statistical weights may result in an increase of the variance of the results.
247 For the applications at hand, we did not find this issue to be limiting.

248

3.2 The Method of Null or Delta Collisions

We begin by recalling a simple and very efficient method to simulate the transport of energy in an arbitrarily scattering and absorbing medium, referred to as the method of null or delta collisions (Lux & Koblinger, 1991). The starting point is the radiative transfer equation:

$$(\partial_t + c\mathbf{k} \cdot \nabla + \tau(\mathbf{r})^{-1} + t_a(\mathbf{r})^{-1})e(t, \mathbf{r}, \mathbf{k}) = \tau(\mathbf{r})^{-1} \int p(\mathbf{k}, \mathbf{k}')e(t, \mathbf{r}, \mathbf{k}')dk' \quad (6)$$

where c , τ , t_a and $p(\mathbf{k}, \mathbf{k}')$ refer to the energy velocity, the scattering mean free time, the absorption time and the scattering pattern, respectively. The integral on the right-hand side is carried over all the directions of propagation. We remark that Eq. (6) is equivalent to the following modified transport Eq.:

$$(\partial_t + c\mathbf{k} \cdot \nabla + \tau(\mathbf{r})^{-1} + t_a(\mathbf{r})^{-1} + \tau_\delta(\mathbf{r})^{-1})e(t, \mathbf{r}, \mathbf{k}) = \tau(\mathbf{r})^{-1} \int p(\mathbf{k}, \mathbf{k}')e(t, \mathbf{r}, \mathbf{k}')dk' + \tau_\delta(\mathbf{r})^{-1} \int \delta(\mathbf{k}, \mathbf{k}')e(t, \mathbf{r}, \mathbf{k}')dk' \quad (7)$$

249

which features a new scattering process with pattern $\delta(\mathbf{k}, \mathbf{k}')$ (the delta function on the

250

unit sphere) and mean free time $\tau_\delta(\mathbf{r})$. This new process is characterized by the prop-

251

erty that it leaves the propagation direction unchanged. It is worth emphasizing that

252

such delta-collisions or null-collisions do not modify the statistics of true physical scat-

253

tering events. Because the scattering coefficient of delta-collisions is entirely arbitrary,

254

we may always adjust it in a way such that $\tau_\delta(\mathbf{r})^{-1} + \tau(\mathbf{r})^{-1} + t_a(\mathbf{r})^{-1} = \tau_e^{-1}$, where

255

the extinction time τ_e is *fixed*. By adding the new scattering process, we have in effect

256

turned a possibly very complicated medium into a much simpler one where the extinc-

257

tion length is constant. This method has been implemented by van Dinther et al. (2020)

258

to model the scattering of seismic waves across the North Anatolian fault zone. The price

259

to be paid is that one has to simulate more scattering events than in the original prob-

260

lem. However, in the perspective of computing sensitivities, this is not necessarily a draw-

261

back. Indeed, as shown below, all the contributions to the sensitivity come exclusively

262

from collision points in the modified numerical scheme. Fig. 1 shows a graphical repre-

263

sentation of this method.

264

3.3 Sensitivity Computations

We begin by noting that in the numerical simulations, absorption is treated as a phonon capture event, which puts it on the same footing as a scattering event. Indeed,

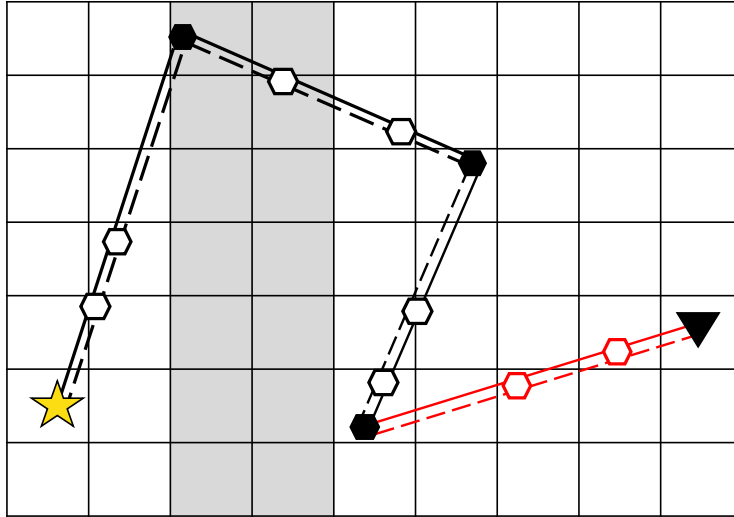


Figure 1. Graphical representation of the flexible Monte Carlo simulation employed in this study. A “true” phonon is propagating through a reference medium from the source (yellow star) to the detector (black triangle). The propagation path of the true phonon is depicted as a solid line. A “virtual” phonon is propagating in a perturbed medium and follows the exact same trajectory, depicted by the dashed line. Between source and detector, the phonons experience delta and physical scattering events (or collisions), indicated by the open and black hexagonals respectively. This implies that we simulate more collisions than there are physical collisions. At every collision we (1) update the weights of the phonons, taking into account the non-uniformity, and (2) compute the sensitivities. The red color highlights the last part of the trajectory toward the detector; in the shown example after three scattering events. The regular grid is indicated by the horizontal and vertical black lines. The simulation can take into account laterally varying scattering properties, represented by the darker pixels. For the simulations this only implies that the phonon weights at the collisions are updated differently.

it is important to keep in mind that the extinction time incorporates the three possible types of interactions: physical scattering, delta scattering and absorption. Rather than terminating the phonon history after an absorption event, we assign a weight w to the particle. At each collision w is multiplied by a factor equal to the local “survival” probability of the phonon $1 - t_a(\mathbf{r})^{-1}/\tau_e^{-1}$. That this procedure correctly models the exponential decay of the intensity along its path may be demonstrated heuristically as follows. Consider two neighbouring points on the ray path of a seismic phonon and denote by s a spatial coordinate on the ray. If the path length δs is sufficiently small, we may neglect multiple collision events. In this scenario, either the phonon propagates freely over δs , or it suffers from an additional collision upon which its weight is updated. Hence we have on average:

$$w(s + \delta s) = w(s) \left(1 - \frac{\delta s}{c\tau_e} \right) + w(s) \left(1 - \frac{t_a(s)^{-1}}{\tau_e^{-1}} \right) \frac{\delta s}{c\tau_e} \quad (8)$$

where we approximate the scattering probability by $(c\tau_e)^{-1}\delta s$. Using a Taylor expansion of the left-hand side, simplifying and rearranging terms we obtain:

$$\frac{dw(s)}{ds} = -\frac{w(s)}{ct_a(s)} \quad (9)$$

265 which proves the statement. The same line of reasoning will be used below to calculate
 266 the contribution of the path from the last scattering event to the detector.

Thanks to these preliminaries, it is now straightforward to apply the differential Monte Carlo method to our problem. As an illustration, let us consider the impact of a scattering perturbation $\delta\tau(\mathbf{r})^{-1}$. Again it is conceptually convenient to consider two phonons: a real phonon propagating in the reference medium and an imaginary phonon propagating in the perturbed medium. We shall also require that the perturbed and unperturbed media have the same extinction time τ_e . Since this parameter can be arbitrarily chosen, this condition can always be fulfilled. By imposing the equality of the extinction time in the reference and perturbed medium, we remove any change of the weight of the virtual phonon in between two collisions. Furthermore, our choice imposes that the rate of delta collisions in the perturbed medium be given by $\tau_\delta^{-1} - \delta\tau(\mathbf{r})^{-1}$. As a consequence, both delta collisions and physical scattering events contribute to the sensitivity to a scattering perturbation. Following the same reasoning as in the derivation of Eq. (5), the weight of the virtual phonon after a delta collision at point \mathbf{r} is updated

as follows:

$$\begin{aligned}
 w(\mathbf{r}) &\rightarrow w(\mathbf{r}) \times \frac{\tau_\delta(\mathbf{r})^{-1} - \delta\tau(\mathbf{r})^{-1}}{\tau_e^{-1}} \times \frac{\tau_e^{-1}}{\tau_\delta(\mathbf{r})^{-1}} \\
 &\rightarrow w(\mathbf{r}) \left(1 - \frac{\delta\tau(\mathbf{r})^{-1}}{\tau_\delta(\mathbf{r})^{-1}} \right)
 \end{aligned} \tag{10}$$

This last equation highlights that the rate of imaginary collisions must always be strictly positive. The same reasoning applied to a physical scattering event yields:

$$w(\mathbf{r}) \rightarrow w(\mathbf{r}) \left(1 + \delta\tau(\mathbf{r})^{-1} / \tau(\mathbf{r})^{-1} \right) \tag{11}$$

267 Comparing Eq. (5) with Eq. (10)-(11), it is clear that what our method does in effect
 268 is to calculate the line integral in (5) by a Monte Carlo approach, where the imaginary
 269 collisions serve as sample points for the quadrature. It is however worth noting that we
 270 did not make any smallness assumption in the derivation of Eq. (10)-(11). The case of
 271 a perturbation of absorption may be treated exactly along the same lines. We find that
 272 at imaginary collisions, Eq. (10) applies with the substitution $\delta\tau(\mathbf{r})^{-1} \rightarrow \delta t_a(\mathbf{r})^{-1}$.

273 The last point to be discussed concerns the treatment of the return probability of
 274 the phonon from the last scattering event at \mathbf{r} to the detector at \mathbf{d} in the method of par-
 275 tial summations of Hoshiya (1991). The score (or contribution) of the phonon involves
 276 the factor $e^{-\int_{\mathbf{r}}^{\mathbf{d}} (t_a(\mathbf{x})^{-1} + \tau(\mathbf{x})^{-1}) c^{-1} dx}$ which represents the probability for the phonon to
 277 propagate from \mathbf{r} to \mathbf{d} (or beyond) without absorption or physical collisions. It is clear
 278 that any perturbation of attenuation properties affect the line integral. We could of course
 279 compute this contribution by computing numerically the integral but we would then lose
 280 the benefits of the transfer of the sensitivity to collision points. To remedy the difficulty,
 281 we replace the numerical quadrature by the following Monte-Carlo procedure:

- 282 1. Starting from position \mathbf{r} , randomly select the distance L to a new collision point
 283 on the ray connecting the last scattering point to the detector. Recall that the pdf
 284 of L is simply given by $(\tau_e c)^{-1} \exp(-(\tau_e c)^{-1} L)$.
- 285 2. At the collision point, modify the weight of the phonon by the factor $\tau_\delta(r)^{-1} / \tau_e^{-1}$.
- 286 3. Compute the factors affecting the sensitivities to scattering (or absorption) fol-
 287 lowing Eq. (10).
- 288 4. Repeat (1) until the phonon has traveled beyond \mathbf{d}

289 Steps (1)-(2) simulate the propagation of the phonon from \mathbf{r} to \mathbf{d} in a way such that only
 290 delta collisions can occur. The process is enforced by decreasing the weight of the par-
 291 ticle by the factor $\tau_\delta(r)^{-1} / \tau_e^{-1}$ at each collision. That the weight of the particle decreases

292 on average as desired can be easily established by following the same heuristic argument
 293 as in the derivation of Eq. (8). In step (3), we assume again that the total attenuation
 294 is the same in the reference and perturbed medium. Eq. (10) is therefore directly ap-
 295 plicable to the computation of the sensitivity to scattering (or absorption) perturbation
 296 on the path connecting \mathbf{r} to \mathbf{d} .

297 In numerical applications, the kernels are discretized onto pixels whose dimensions
 298 fix the lower bound for the spatial resolution that may be achieved in an inversion. As
 299 a consequence, the discretized kernels introduce both spatial and temporal averaging as
 300 compared to their analytical counterparts (Mayor et al., 2014). A positive consequence
 301 is that all singularities are automatically regularized, which allows for a more straight-
 302 forward application of the kernels. Furthermore, whereas analytical kernels are attached
 303 to the uniform reference medium, the Monte-Carlo approach lends itself naturally to an
 304 iterative linearized inversion procedure. From a numerical perspective, the most impor-
 305 tant feature of our method is the high degree of flexibility, which allows one to very sim-
 306 ply model arbitrary non-uniform scattering and absorbing medium, including the pres-
 307 ence of discontinuities in the model parameters. We believe that this simplicity largely
 308 balances the slowdown entailed by the simulation of artificial scattering events.

309 For the simulations shown in this manuscript we use a grid of 76-by-76 pixels, where
 310 each of the pixels has a dimension of 4-by-4 km. The kernel is evaluated every second,
 311 up to a maximum lapse-time of 120 s. The final temporal resolution, however, is 5 s, due
 312 to the application of a 5 s moving window to average the kernels and reduce the statis-
 313 tical fluctuations. The total number of phonons simulated for each model is 4×10^9 . The
 314 distance between the sources, R , equals 32 km for most models (uniform and half-space
 315 case), with the placement of the sources at the center of the pixels. For all simulations
 316 the full grid space has a uniform value for the intrinsic quality factor $Q_i^{umi} = 100$, based
 317 on values recently derived for a normal crustal setting in Turkey, in the vicinity of the
 318 Izmit rupture zone (e.g. van Dinther et al., 2020). The scattering mean free path varies
 319 depending on the model.

320 **4 Sensitivity Kernels for Non-uniform Scattering Media**

321 In this section we discuss the effect of the scattering distribution on the sensitiv-
 322 ity kernels. Guided by the results obtained in a volcanic setting, we introduce the phys-

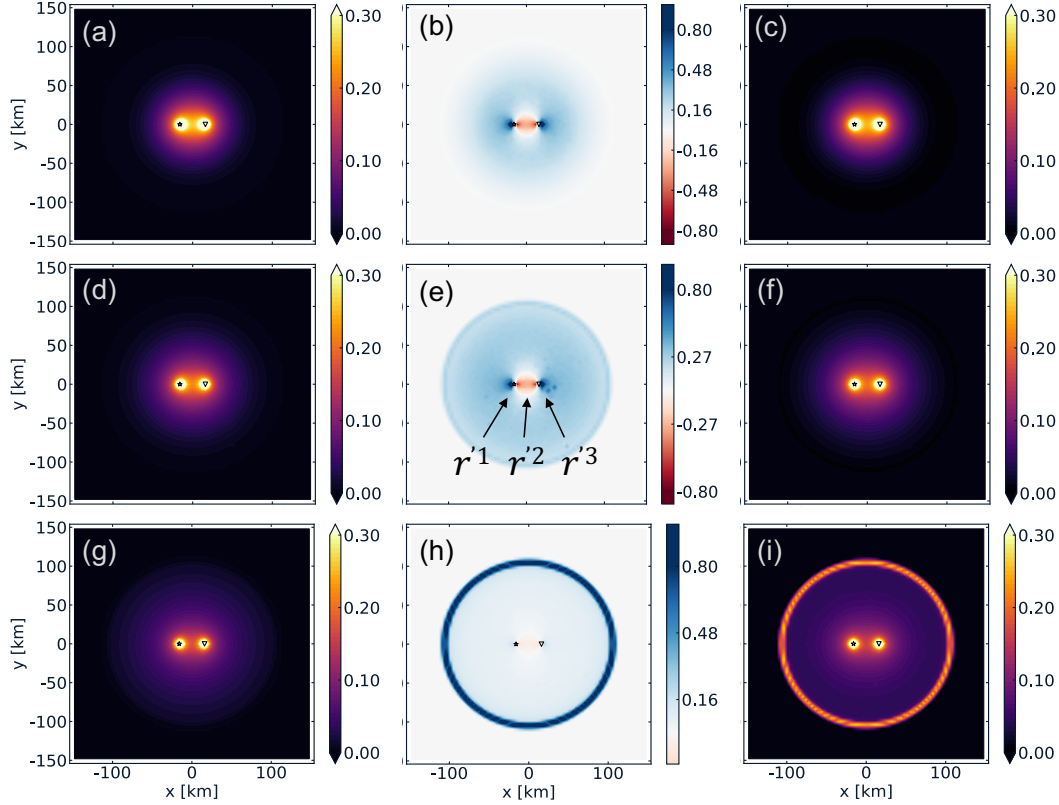


Figure 2. Sensitivity kernels for uniform scattering media at 100 s lapse-time. The columns show K_{tt} , K_{sc} and K_{dc} , respectively. The scattering mean free path increases from top to bottom: ℓ_1 , $2 \times \ell_1$, $8 \times \ell_1$, with $\ell_1 = 30$ km. The inter-source distance, $R_0 = 32$ km. The annotations r'^1 - r'^3 point to positive, negative and positive sensitivity along the line connecting the sources, respectively. All kernels are normalised with respect to the maximum value. Note that for K_{sc} to color bar is symmetric around zero, with red as negative and blue as positive sensitivities, respectively.

323 ical interpretation for each of the three different kernels. The second context for which
 324 we investigate the implications of non-uniform scattering strength on the sensitivities
 325 is for a model with two half-spaces. This case is illustrated with the aid of two paramet-
 326 ric studies, which facilitate the interpretation of the kernels. We will finish this section
 327 with an application to a fault zone model.

328 To facilitate the discussion we compare the results for all three non-uniform mod-
 329 els to the kernels for uniform media. The latter are shown in Fig. 2 at a lapse-time of
 330 100 s for increasing scattering strengths. The columns from left to right show K_{tt} , K_{sc}

Table 1. Overview of intensities and fluxes.

Symbol	Description
I_s	Intensity from the source: forward intensity
I_d	Intensity from the detector: backward intensity
$I_{s,d}^{\Delta\ell}$	Secondary and delayed intensity induced by a strong scattering region
$I_{s,d}^b$	Intensity along the ballistic path between source and detector
\mathbf{J}_s	Energy flux from the source
\mathbf{J}_d	Energy flux from the detector
$\mathbf{J}_{s,d}^{\Delta\ell}$	Secondary and delayed energy flux induced by a strong scattering region
$\mathbf{J}_{s,d}^b$	Energy flux along the ballistic path between source and detector

331 and K_{dc} , respectively. The results obtained for a reference medium, with $\ell_1 = 30$ km, is
332 shown at the top row. The scattering mean free path varies over orders of magnitude
333 in the Earth, therefore we compare the reference medium with weaker scattering media.
334 The middle and lower rows of Fig. 2 show the results for increasing ℓ : $2 \times \ell_1$ and $8 \times \ell_1$,
335 respectively. The epicentral distance is set to $R = 32$ km. The numerical results shown
336 in Fig. 2 will serve as guides to understand the more complex cases associated to non-
337 uniform scattering properties.

338 4.1 Volcanic Setting

339 Fig. 3 shows the kernels for a source and receiver that are 47 km apart, at 40 s (up-
340 per row) and 80 s (lower row) lapse-times, in the vicinity of a volcano. The volcano, char-
341 acterized by strong scattering, has a scattering mean free path of 2 km and a radius of
342 6 km. These values are based on the findings of Hirose et al. (2019) at the Sakurajima
343 volcano in Japan. The surrounding crust has a weaker scattering strength with $\ell = 150$
344 km, and for simplicity the intrinsic absorption is considered uniform with $Q_i = 100$.

345 A couple of observations stand out from Fig. 3. First, the travel-time and decor-
346 relation kernels are very dissimilar. Second, the volcano appears to be a reflector for the
347 intensities at early lapse-times. To explain these observations and improve the under-
348 standing of the kernels we will discuss all three kernels separately and compare them to

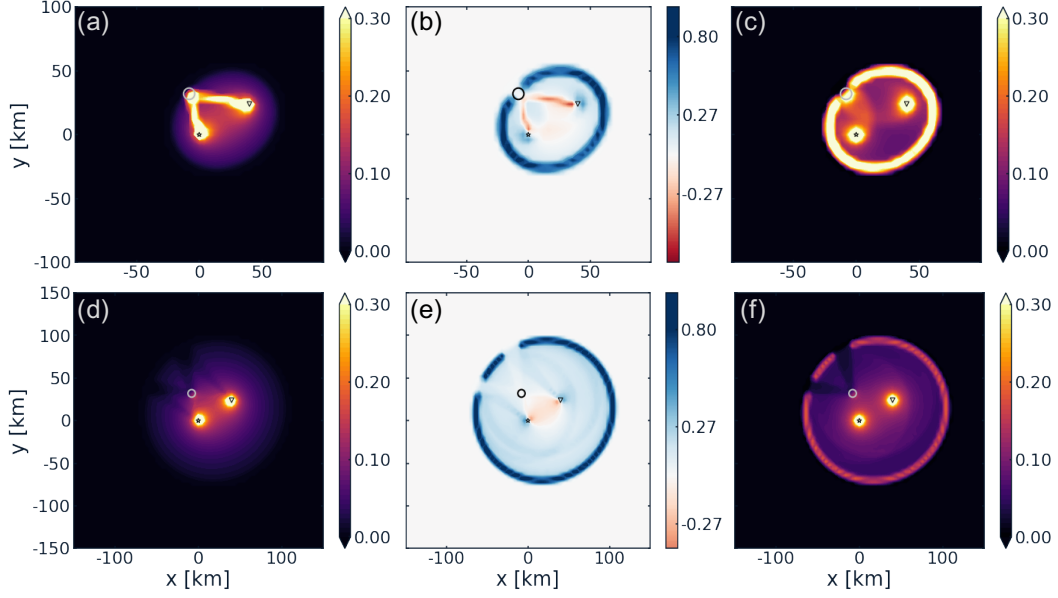


Figure 3. Sensitivity kernels for volcanic setting, for lapse-time of 40 s (upper) and 80 s (lower). The columns show K_{tt} , K_{sc} and K_{dc} respectively. The volcano is depicted as a circle with radius 6 km and $\ell_v = 2$ km, outside the volcano $\ell = 150$ km. The inter-source distance is approximately 47 km. Note that axis extent is not the same for 40 s (± 100 km) and 80 s (± 150 km). All kernels are normalised with respect to the maximum value. The color bar for K_{sc} is symmetric around zero.

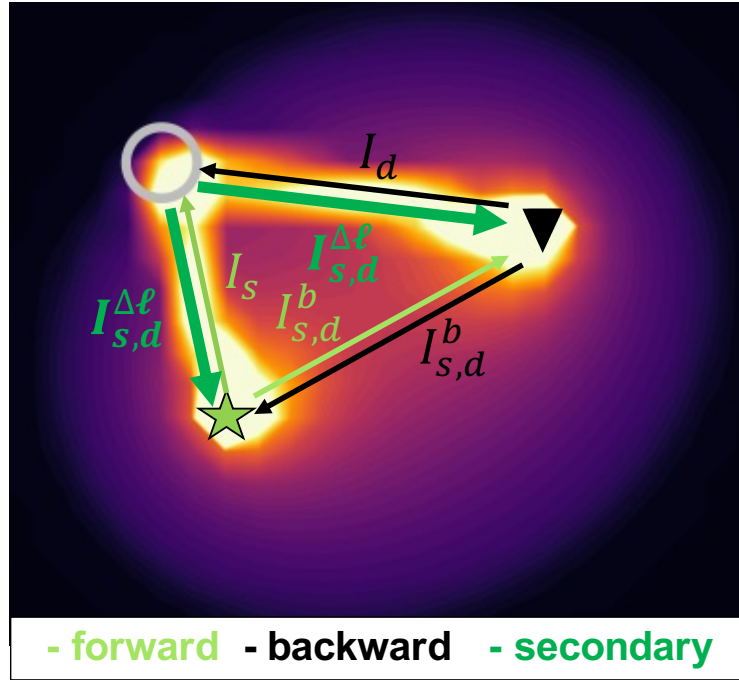


Figure 4. Depiction of the specific intensities controlling K_{tt} in a volcanic setting. The green star depicts the source and the black triangle the receiver. The former and the latter are referred to as source of forward and source of backward intensity, respectively. The grey circle shows the location of the volcano. Specific intensity I_s (I_d) propagates from the source of forward intensity (source of backward intensity) to the volcano, respectively. Back-scattered energy is indicated as $I_{\Delta\ell}$. It originates from one source and propagates via the volcano to the other source (and vice versa), but it also has an energy contribution coming from one source and scatters back to the same source. Both sources emit intensities into all directions, also on the direct path between them, as indicated by I_s and I_d .

349 the uniform model as reference, starting with the travel-time kernel, then the decorre-
 350 lation kernel and finally the scattering kernel.

351 As defined in Eq. (1), K_{tt} is dependent on the dominant propagation direction of
 352 the waves. There are two specific intensities contributing to the travel-time kernel, com-
 353 ing from two different primary sources: (1) the forward intensity, from the source toward
 354 the perturbation; and (2) the backward intensity, from detector toward the perturba-
 355 tion. In the application part of this manuscript we refer to the first source as the “source
 356 of forward intensity” or “forward source”, while the latter will be referred to as the “source
 357 of backward intensity” or “backward source” from hereafter.

358 Where the forward and backward intensities are simultaneously high and propa-
 359 gating in opposite direction, the travel-time kernel shows high sensitivities, as dictated
 360 by the convolution of specific intensities in the numerator of Eq. (1). In the uniform case,
 361 there are only two sources to be considered I_s and I_d . In the case of a localized pertur-
 362 bation with high scattering contrast, energy may be back-scattered by the heterogene-
 363 ity, giving rise to a secondary and delayed intensity $I_{s,d}^{\Delta\ell}$.

364 The key intensities for the volcanic setting are shown in the Fig. 4. As a result of
 365 the highly scattering volcano, specific intensities propagate from the forward source to-
 366 wards the volcano (green I_s), and scatter from the volcano to the source of backward in-
 367 tensity (green $I_{s,d}^{\Delta\ell}$). Similarly, intensities propagate from the source of backward inten-
 368 sity to the volcano (black I_d) and from the volcano to the forward source (black $I_{s,d}^{\Delta\ell}$).
 369 For 40 s lapse-time, we can therefore explain the high sensitivities on the paths connect-
 370 ing the sources via the volcano, by the high specific intensities that are opposite in di-
 371 rection on those paths. For the uniform case we observe higher sensitivities around and
 372 between the sources, especially for strong scattering media the sensitivity on the direct
 373 path between the sources increases (Fig. 2a). This direct path is less favorable in the vol-
 374 canic setting, because the specific intensities are much higher on the paths that connect
 375 the sources of forward and backward intensity via the volcano. In other words, for early
 376 lapse-times the volcano acts as a secondary and delayed source of intensity and there-
 377 fore promotes an additional path favorable to energy transport between the primary sources,
 378 which is not present in the uniform case. For later lapse-time (80 s; Fig. 3d), K_{tt} resem-
 379 bles its equivalent for a uniform medium. Yet the imprint of the volcano remains as the
 380 strongly scattering zone prevents ballistic energy to travel through and causes a “shadow”

381 in the kernel for late lapse-times. The partly removed ballistic energies originating from
 382 both sources cause an ‘M’-shaped shadow to appear, which deforms and gradually dis-
 383 appears with lapse-time. At later lapse-times the effect of the volcano starts to disap-
 384 pear as the portion of multiply scattered energy increases, resulting in a probability in-
 385 crease for two specific intensities to propagate in opposite directions in these areas. An-
 386 imations of the three different kernels with increasing lapse-time for the volcanic setting
 387 can be found in the supporting information, Movie S1-S3.

388 The decorrelation kernels appear rather different from their travel-time counter-
 389 parts. Indeed, Eq. (2) shows that K_{dc} does not depend on the specific intensities, but
 390 on the mean intensities instead. The decorrelation kernel will thus be high where the mean
 391 intensities emitted by the forward and backward sources are simultaneously high. This
 392 condition is far less stringent than the analogous one for the travel-time kernel. For this
 393 reason the travel-time and decorrelation kernel are dissimilar. The K_{dc} for the volcanic
 394 case at early lapse-time (40 s; Fig. 3c) shows high sensitivity around the sources and on
 395 the single scattering ellipse. Additionally, high sensitivity can be observed in the halos
 396 surrounding the forward source and volcano, and the backward source and volcano, re-
 397 spectively. Energy becomes rapidly diffuse when it enters into the volcano, therefore the
 398 high intensities inside the volcano are on the side that faces the sources; hence a bend
 399 in the single scattering ellipse can be observed (Fig. 3c). For later lapse-times (80 s; Fig.
 400 3f), K_{dc} appears similar to the uniform K_{dc} (Fig. 2i). Nevertheless, the imprint of the
 401 strongly scattering volcano remains, causing a shadow on the single-scattering ellipse of
 402 the decorrelation kernel.

The last kernel to be considered is the scattering kernel (Fig. 3 b&e). In order to
 understand its structure in the vicinity of a volcano, we will first discuss the pattern of
 K_{sc} for the uniform case (e.g. Fig. 2e). As mentioned in Section 2, the scattering ker-
 nel has positive and negative sensitivities. The signs in the kernels can be understood
 in the following way. If we imagine point sources at the locations of the source and de-
 tector that inject energy into the medium at time $t = 0$. The energy transport gives rise
 to fluxes going from a source of forward intensity to a source of backward intensity (and
 vice versa). At late lapse-times, which is at several scattering mean free times τ (where
 $\tau = \ell/c$ with c as wave velocity), the energy is diffuse. Previously, it has been shown
 in the literature that in the diffusion regime the scattering kernel is controlled by the scalar
 product of the energy flux vectors (\mathbf{J}) for sources located at the position of the forward/backward

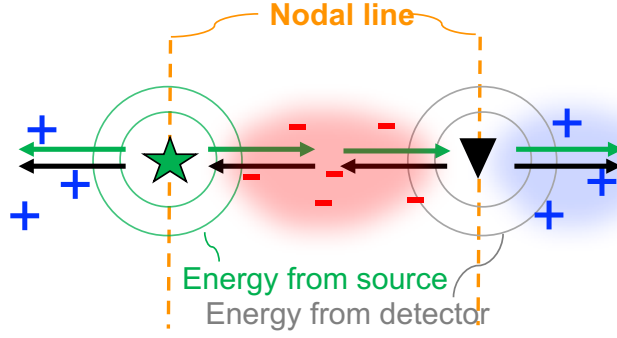


Figure 5. Graphical interpretation of the fluxes explaining the pattern of the scattering kernel for a uniform scattering medium. Energy from the source (green star) is emitted in all directions, indicated by the green circles. The green arrows depict the fluxes along the line connecting the source and detector. Similarly, energy from the detector (black triangle) is emitted in all directions, indicated by the gray circles. The black arrows depict fluxes from the detector in the source-detector line. In the space between source and detector the fluxes have opposite direction, resulting in negative sensitivity (red '-'). In the outside spaces, the fluxes from source and detector have similar directions, resulting in positive sensitivity to scattering (blue '+'). The nodal lines are depicted by the orange dashed line.

intensity sources (e.g. Arridge, 1995; Wilson & Adam, 1983; Mayor et al., 2014):

$$\lim_{t \rightarrow +\infty} K_{\text{sc}}(\mathbf{r}; \mathbf{r}'; \mathbf{r}_0; t) = D(1 - g) \int_0^t \mathbf{J}_{\text{fwd}}(\mathbf{r}'; \mathbf{r}; t - t') \cdot \mathbf{J}_{\text{bwd}}(\mathbf{r}'; \mathbf{r}_0; t') dt' \quad (12)$$

403 with g denoting the mean cosine of the scattering angle. Note that Eq. (12) is not strictly
 404 valid quantitatively, although qualitatively it is correct. Hence, Eq. (12) is rather an ap-
 405 proximate than an exact formula, which in practice explains the pattern of the scatter-
 406 ing kernel accurately. It contains the essential physics and therefore we employ this for-
 407 mulation heuristically to analyse our results. Fig. 5 shows a schematic diagram of the
 408 fluxes in the scattering kernel for a uniform medium. The energy flux from the source
 409 flows away in all directions from the source and similarly for the detector. On the di-
 410 rect path between source and detector, these fluxes have opposite direction while on the
 411 outside the fluxes have similar directions. As a consequence of the scalar product in Eq.
 412 (12), the fluxes in opposite direction lead to an area of negative sensitivity to scatter-
 413 ing on the direct path. Here, the probability of energy reaching the other source is de-
 414 creased. On the outer side of the direct path between the sources, there is a positive sen-
 415 sitivity due to the scalar product of the fluxes in similar direction. In these positive ar-

416 eas the probability of energy reaching the other detector is increased. The line that di-
 417 vides the positive and the negative sensitivities in the vicinity of the source/detector is
 418 referred to as the nodal line (Fig. 5). To describe the pattern of the scattering kernel
 419 in more detail we imagine placing additional scatterers at three locations in Fig. 5. If
 420 an extra scatterer would have been placed left of the forward intensity source, the chances
 421 of additional energy reaching the backward intensity source would have been increased
 422 due to the possibility of back-scattering. Due to reciprocity, this same argument holds
 423 for an additional scatterer located right of the backward source. On the other hand, neg-
 424 ative scattering sensitivity between the two sources indicates that if an additional scat-
 425 terer would have been placed in the red area, the probability of energy coming from one
 426 source and reaching the other source would decrease.

427 Now that we have discussed the positive and negative signs in K_{sc} for a uniform
 428 medium we continue the discussion about the volcanic case. K_{sc} will be high in abso-
 429 lute value where the actual energy fluxes are simultaneously large and aligned, either par-
 430 allel or anti-parallel. Consequently, an additional energy transport channel in the scat-
 431 tering kernel for early lapse-times (40 s; Fig. 3b) appears, connecting the two sources
 432 via the volcano. The negative sensitivity on the direct path between the sources is also
 433 present, albeit weaker than on the path via the volcano. Similarly as for K_{tt} , this is due
 434 to smaller energy current vectors on the direct path. Furthermore, we can observe sim-
 435 ilarities between the decorrelation and the scattering kernel, for both the early and late
 436 lapse-times. In particular, the single scattering ellipse and the halos of high sensitivity
 437 between either source and volcano, which are also present in K_{dc} , can be observed in Fig.
 438 3(b & e). Although K_{sc} for the volcanic setting at late lapse-time (80 s) resembles its
 439 equivalent for a uniform model, the effect of the volcano remains.

440 4.2 Two Half-spaces Setting

441 In the northeastern region of Honshu, Japan, Yoshimoto et al. (2006) estimated the
 442 spatial distribution of attenuation. These authors found that the contrast of properties
 443 between the front-arc and the back-arc is approximately equal to two for both absorp-
 444 tion and scattering. With this in mind, we explore the effect of non-uniform scattering
 445 properties on the coda wave sensitivities, in a medium composed of two half-spaces. A
 446 tectonic setting with a strike-slip fault that caused two different materials on each side
 447 of the fault to be in contact may also be considered in this context. For all half-space

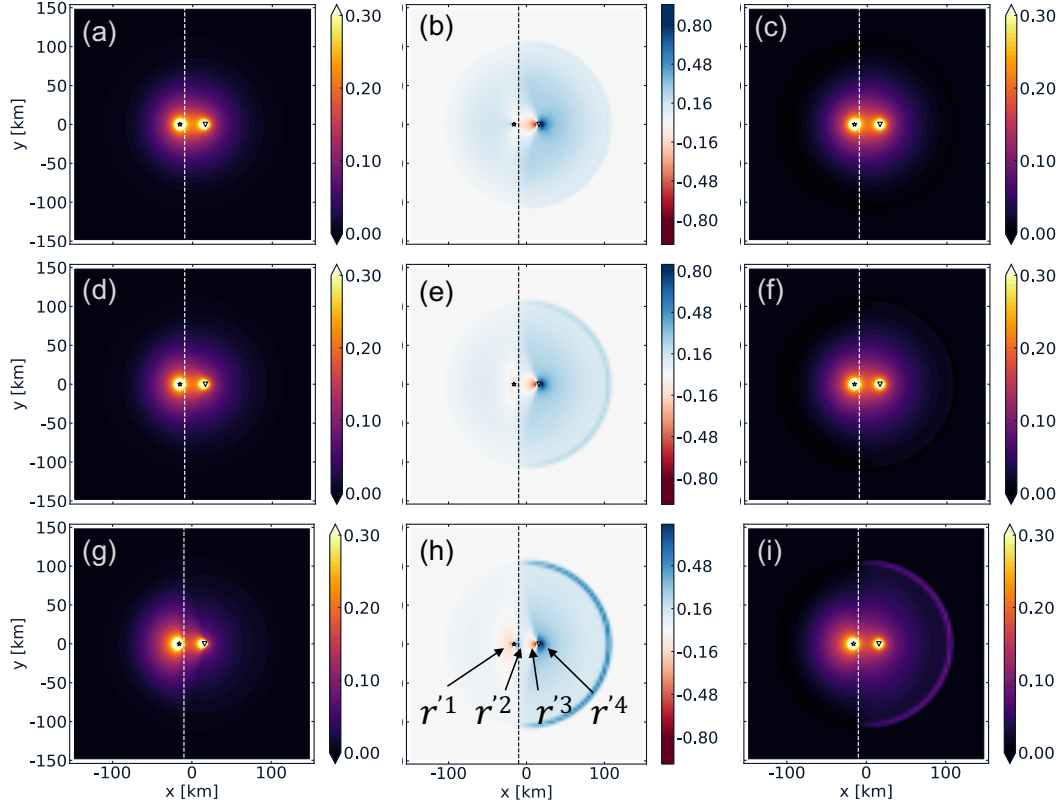


Figure 6. Sensitivity kernels for two half-spaces at 100 s lapse-time. The columns show K_{tt} , K_{sc} and K_{dc} , respectively. The left half-space has a fixed scattering mean free path of ℓ_1 . The scattering mean free path in the right half-space increases from top to bottom: $2\times\ell_1$, $3\times\ell_1$, $8\times\ell_1$, with $\ell_1 = 30$ km. The source-detector distance R_0 is set to 32 km. The annotations r'^1 - r'^4 point to negative, positive, negative and positive sensitivity along the line connecting source and detector, respectively. All kernels are normalised with respect to the maximum value. Note that for K_{sc} the color bar is symmetric around zero, with red as negative and blue as positive sensitivities, respectively.

448 models, ℓ_1 is the smallest scattering mean free path we consider, it is kept constant at
 449 30 km and consistently on the left side of the model. The right half-space has weaker
 450 scattering ($\ell_1 < \ell_2$), where ℓ_2 is chosen to differ by a factor of 2, 3, or 8 from ℓ_1 . The
 451 interface delimiting the two half-spaces coincides exactly with the boundary between two
 452 pixels. d represents the distance from the forward intensity source to this interface.

453 The sensitivity kernels with sources in opposite half-spaces are shown in Fig. 6, for
 454 $t = 100$ s. From the top to the bottom row, we show the results for increasing scatter-

455 ing contrast between ℓ_1 (the reference half-space, on the left) and ℓ_2 (the right half space):
 456 $\ell_2 = 2 \times \ell_1$ (upper), $\ell_2 = 3 \times \ell_1$ (middle) and $\ell_2 = 8 \times \ell_1$ (lower). The dashed line, placed
 457 at 6 km from the source of forward intensity, depicts the boundary between the two half-
 458 spaces. The inter-source distance is the same as for the uniform cases, $R = 32$ km. We
 459 can observe that all three kernels for all degrees of scattering contrast are asymmetric,
 460 with the asymmetry intensifying as the contrast between ℓ_1 and ℓ_2 increases. In the travel-
 461 time kernel there is a strong effect of back-scattering, especially for the case where $\frac{\ell_2}{\ell_1}$
 462 $= 8$ (Fig. 6 g). The sensitivities appear higher in the strong scattering half-space. For
 463 the decorrelation kernels we can observe the increased difference between dominant trans-
 464 port regimes for increasing scattering contrasts. For example in Fig. 6 (i) the dominant
 465 type of wave propagation in the left half-space is diffusion. Therefore, the mean inten-
 466 sity and thus the sensitivity is concentrated in a larger area around the source. However,
 467 in the right half-space the propagation regime is essentially ballistic, consequently, strong
 468 sensitivities can be observed on the single scattering ellipse. The most striking obser-
 469 vation from Fig. 6 is the “flipped” pattern in the scattering kernels (w.r.t. the pattern
 470 for the uniform case), for $\frac{\ell_2}{\ell_1} \geq 3$ (Fig. 6 e and h). In the strong scattering half-space
 471 (with ℓ_1), the sensitivity to an additional scatterer left of the source is negative (r'^1 in
 472 panel h), while it was positive for the uniform case (Fig. 2e). On the other side of the
 473 source (r'^2) it is positive, while for the uniform case it was negative. The sensitivity to
 474 an additional scatterer in the weaker scattering half-space (with ℓ_2) appears similar to
 475 that for the uniform case in the vicinity of the source, with negative sensitivity at r'^3
 476 and positive at r'^4 , regardless of the scattering strength or contrast.

477 Fig. 6 shows that for a certain scattering contrast, the pattern of the scattering kernel
 478 changes significantly w.r.t. the uniform kernel. As explained for the volcanic setting,
 479 this is due to the active fluxes: from the forward source, \mathbf{J}_s , and the backward source,
 480 \mathbf{J}_d , but also the flux governed by the contrast in scattering $\mathbf{J}_{s,d}^{\Delta\ell}$. In order to improve our
 481 understanding of the “flipped” scattering kernel for models with two half-spaces and to
 482 gain more insight into the factors that affect the active fluxes we perform two additional
 483 tests. In one test we take four models in which the scattering distribution of the medium
 484 is fixed, but the location of one of the sources rotates. In another parametric test we in-
 485 vestigate the effect of several parameters on the magnitude and directivity of each flux.

486 If we denote the part of \mathbf{J}_s (\mathbf{J}_d) flowing in the direction of the backward source (for-
 487 ward source), respectively, as the direct flux $\mathbf{J}_{s,d}^b$. Then the flux at the sources is a com-

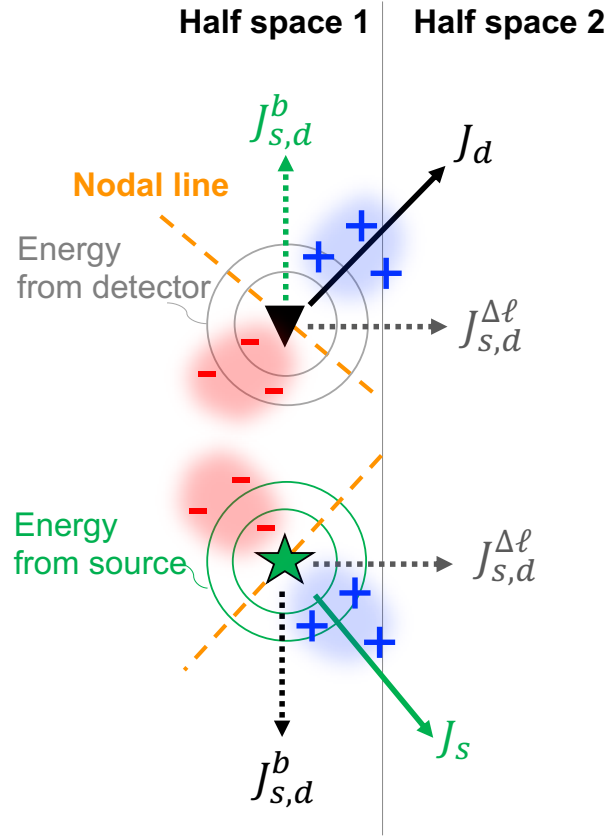


Figure 7. Graphical representation of the active fluxes and K_{sc} in case of a medium with two half-spaces. The fluxes shown in green are from the source of forward intensity. The flux $\mathbf{J}_{s,d}^b$ in green (black) is the part of the energy from the forward source (backward source) in the direction of the backward source (forward source), respectively. The resulting flux at the forward source, \mathbf{J}_s shown in green, (backward source, \mathbf{J}_d shown in black) has contributions from $\mathbf{J}_{s,d}^b$ and $\mathbf{J}_{s,d}^{\Delta\ell}$, respectively. $\mathbf{J}_{s,d}^{\Delta\ell}$ is the flux induced by the contrast in scattering. The nodal line, depicted in orange, separates positive and negative sensitivity to scattering and is perpendicular to the resulting energy flux.

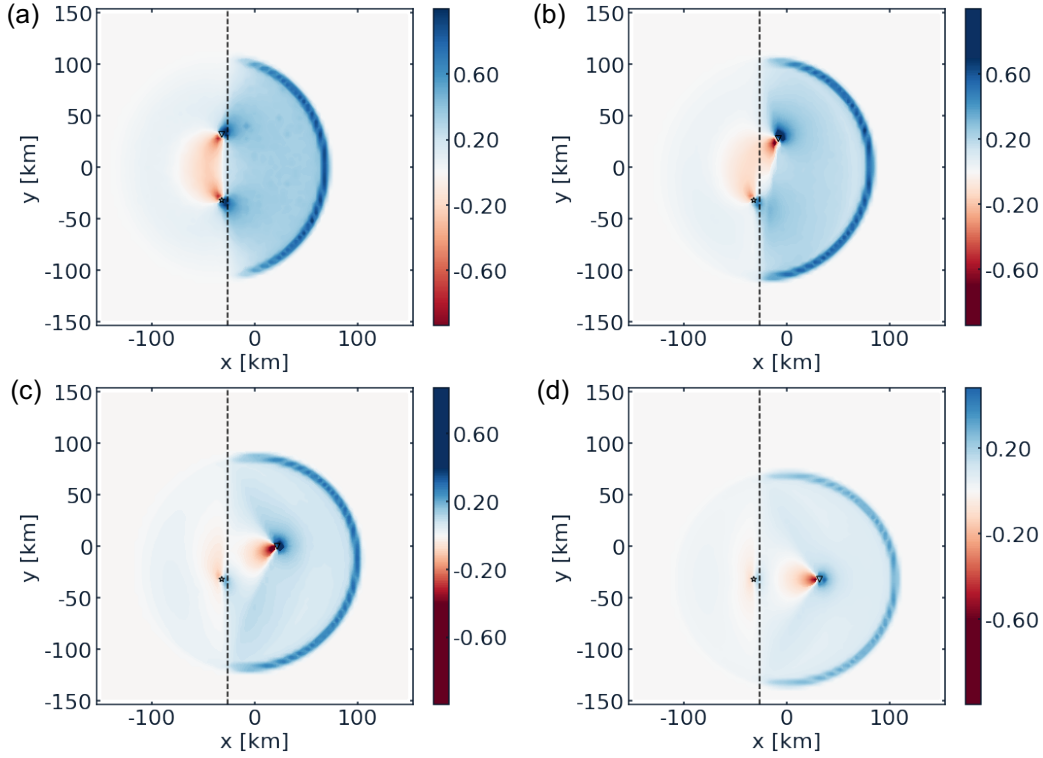


Figure 8. Sensitivity kernels for a half-space setting at 100 s lapse-time. The scattering mean free path for the left (right) half-space is fixed for all panels at ℓ_1 ($8 \times \ell_1$), respectively. The orientation of the line connecting the sources changes gradually from parallel to the boundary to perpendicular to the boundary, from (a) - (d), respectively. To enhance visibility of the kernel pattern the inter-source distance is larger, with $R = 2 \times R_0$. The distance of the leftmost source from the boundary is fixed at 6 km.

488 combination of $\mathbf{J}_{s,d}^b$ and $\mathbf{J}_{s,d}^{\Delta\ell}$, as illustrated in Fig. 7. For the situation in Fig. 7, the mag-
 489 nitude of $\mathbf{J}_{s,d}^{\Delta\ell}$ depends on the contrast of scattering between both half-spaces. The ori-
 490 entation of $\mathbf{J}_{s,d}^{\Delta\ell}$ is perpendicular to the boundary of scattering and is directed from the
 491 stronger scattering half-space towards the weaker scattering half-space. The orientation
 492 of $\mathbf{J}_{s,d}^b$ depends on the positions of the sources, while its magnitude depends on the inter-
 493 source distance and lapse-time.

494 Fig. 8 demonstrates how the direct flux and the flux induced by the scattering con-
 495 trast contribute to the pattern of the scattering kernel. In all four panels the scattering
 496 contrast is fixed, with $\frac{\ell_2}{\ell_1} = 8$, and the orientation of $\mathbf{J}_{s,d}^{\Delta\ell}$ is perpendicular to the scat-
 497 tering boundary. From panel (a) to (d) the location of the upper source changes, but its

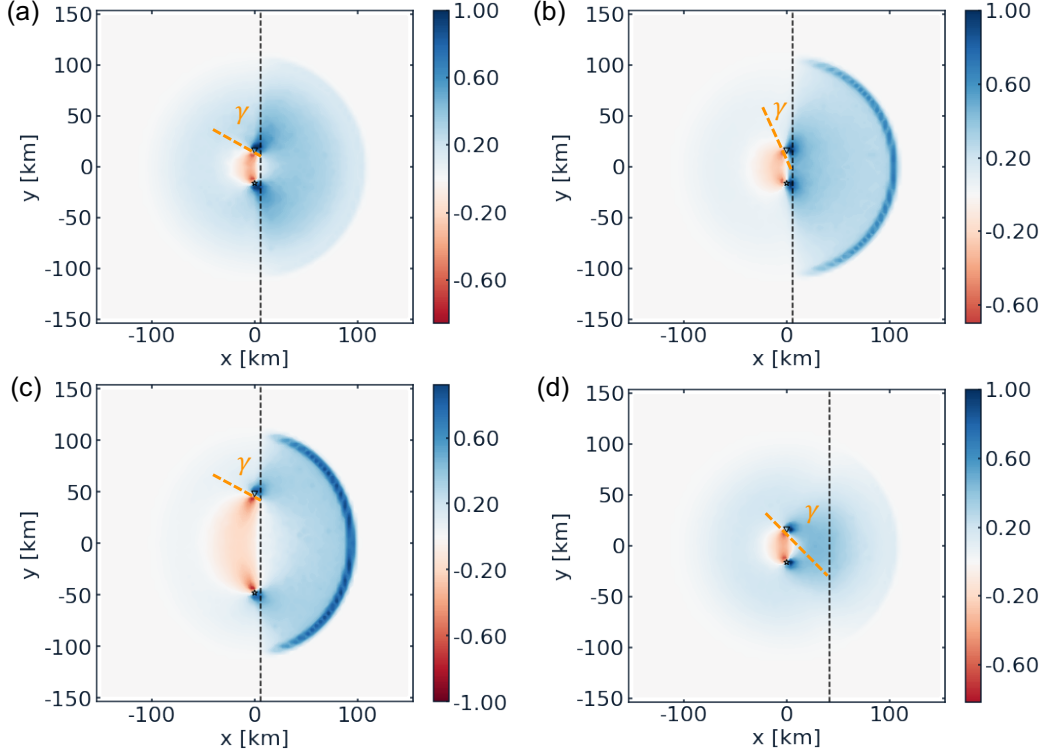


Figure 9. Sensitivity kernels for a half-space setting at 100 s lapse-time. Scattering mean free path of left half-space for all panels is $\ell_1 = 30$ km. Source and detector are placed parallel to half-space boundary. (a) ℓ of right half-space is $2 \times \ell_1$, $R = R_0 = 32$ km and distance to half-space boundary $d = 6$ km. (b) ℓ of right half-space is $8 \times \ell_1$, $R = R_0$ and $d = 6$ km. (c) ℓ of right half-space is $8 \times \ell_1$, $R = 3 \times R_0$ and $d = 6$ km. (d) ℓ of right half-space is $8 \times \ell_1$, $R = R_0$ and $d = 42$ km. γ denotes the angle between the nodal line (orange dashed line) and the half-space boundary. Note that the color bar is symmetric around zero.

498 distance to the lower source is kept constant at $R = 64$ km ($2 \times R_0$). We rotate the line
 499 connecting the two sources from parallel to the boundary (Fig. 8a) to perpendicular to
 500 the boundary (Fig. 8d). This causes the orientation of $\mathbf{J}_{s,d}^b$ to rotate and therefore the
 501 kernel pattern to change from a “twisted” version of the uniform kernel (Fig. 8a and Fig.
 502 7) to a kernel with completely opposite sensitivity in the stronger scattering half-space
 503 (w.r.t. the uniform kernel), as we have already seen in Fig. 6 (h).

504 There are multiple parameters that affect either direction or amplitude of $\mathbf{J}_{s,d}^b$, $\mathbf{J}_{s,d}^{\Delta\ell}$,
 505 and/or the relative contribution of both fluxes and therefore the kernels; a selection is
 506 shown in Fig. 9. The effect in scattering contrast, and as a consequence on $\mathbf{J}_{s,d}^{\Delta\ell}$, can be

507 seen when comparing Fig. 9 (a) where $\ell_2 = 2 \times \ell_1$ with Fig. 9 (b) where $\ell_2 = 8 \times \ell_1$.
 508 If ℓ_2 in the right half-space increases from 2 (panel a) to 8 (panel b) the kernel looks more
 509 asymmetric. Not only is the sensitivity partly focused on the singly scattering ellipse for
 510 the weaker scattering half-space, but also in the vicinity of both sources we observe a
 511 deformation of the kernel w.r.t. the uniform case. The angle γ , between the half-spaces
 512 boundary and the nodal line, decreases. Note that the nodal line is always perpendicular
 513 to the resulting flux at the source, as show in Fig. 5 and 7. The change in γ is due
 514 to the larger $\mathbf{J}_{s,d}^{\Delta\ell}$, which is induced by the increasing scattering contrast. This alters the
 515 magnitude and direction of the flux, despite the unchanged orientation of the individual
 516 fluxes $\mathbf{J}_{s,d}^{\Delta\ell}$ and $\mathbf{J}_{s,d}^b$. Another parameter that affects the pattern of K_{sc} is the inter-
 517 source distance, which directly affects the contribution of $\mathbf{J}_{s,d}^b$ to the flux. For a larger
 518 R the angle γ increases as can be observed when comparing the kernel for $R = R_0$ (panel
 519 b) to $R = 3 \times R_0$ (panel c).

520 Additionally, when comparing Fig. 9(b) to Fig. 9(d) we observe that the distance
 521 of the sources to the boundary of scattering contrast, d , also plays an important role in
 522 the pattern of the kernel. The kernel for larger d (panel d) appears more similar to the
 523 kernel for uniform scattering (e.g. Fig. 2) than the kernel for smaller d (panel b). Thus
 524 the effect of the non-uniformity decreases with increasing d . The lack of sensitivity on
 525 the singly scattering ellipse (panel d) is a consequence of the energy being already dif-
 526 fuse before reaching the weaker scattering half-space. The two tests discussed above show
 527 that we can improve our interpretation of the scattering kernels by understanding the
 528 actual fluxes.

529 Finally, Fig. 10 shows the effect of non-uniform scattering strength on the decor-
 530 relation, travel-time and scattering kernels for a model with sources far away from a bound-
 531 ary of scattering contrast. The sources are placed at a large distance (58 and 90 km) from
 532 the contrast of scattering inside the weaker scattering half-space, where $\ell_1 = 30$ km and
 533 $\ell_2 = \ell_1 \times 8$ km. In the travel-time kernel (Fig. 10a) the strong backscattering effect,
 534 caused by the contrast in scattering, results in a larger sensitivity towards the strong scat-
 535 tering half-space. This is due to the overlap of intensities from the sources, which go to-
 536 ward the left, with the reflected intensity from the half-space that goes to the right. This
 537 travel-time kernel is rather different from the travel-time kernel for the uniform case (Fig.
 538 2), where the sensitivity would have solely been around the two sources. The decorre-
 539 lation kernel shows concentrated sensitivities on the single scattering ellipse, as we have

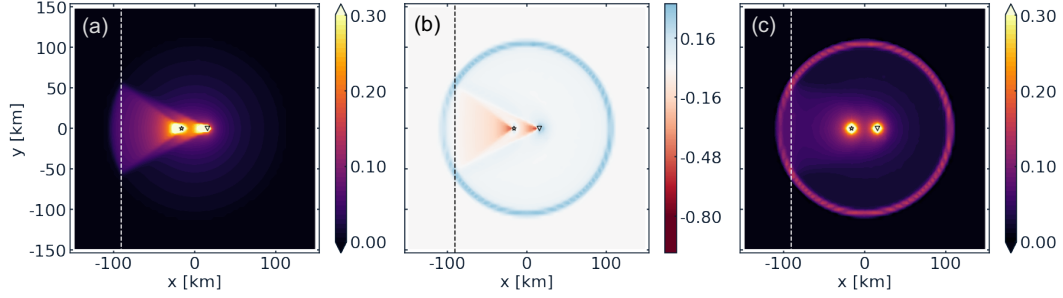


Figure 10. Sensitivity kernels for a model with two half-spaces at 100 s lapse-time, for a setting where the sources are far away from the boundary of scattering contrast (58 and 90 km, respectively). The scattering mean free path in the right half-space is $8 \times \ell_1$, where $\ell_1 = 30$ km. The columns show K_{tt} , K_{sc} and K_{dc} , respectively. All kernels are normalised with respect to the maximum value. The color bar for K_{sc} is symmetric around zero.

540 seen in the uniform weakly scattering medium. The sensitivity of the single scattering
 541 ellipse in the strong scattering half-space is lower due to the stronger diffusion of energy
 542 in the left half-space. Furthermore, higher sensitivities can be explained between the bound-
 543 ary of scattering on the one hand, and the source on the other hand, by the increase of
 544 mean intensities in those areas. Fig. 10 (b) shows that the impact on the scattering ker-
 545 nel is also significant. The contribution of the specific intensities, as in the travel-time
 546 kernel, is clearly visible and results in strong negative sensitivities towards the stronger
 547 scattering half-space. Furthermore, we can observe the single scattering ellipse, as we
 548 have seen in the decorrelation kernels.

549 The results in Fig. 10 thus show that even at large distance from a boundary of
 550 scattering contrast the effect of non-uniform scattering properties on the sensitivity ker-
 551 nels can be significant. It is therefore important to have knowledge about the distribu-
 552 tion of scattering for a large area around one's area of interest, in order to locate changes
 553 of the subsurface correctly.

554 4.3 Fault Zone Setting

555 The last application we consider is a fault zone setting. The parameters are based
 556 on findings for the North Anatolian Fault (van Dinther et al., 2020). We consider a nar-
 557 row fault zone of width = 6.25 km, with $\ell = 10$ km inside and $\ell = 150$ km outside. Fig.
 558 11 shows the resulting kernels for 65 s (upper) and 100 s (lower) lapse-times, respectively.

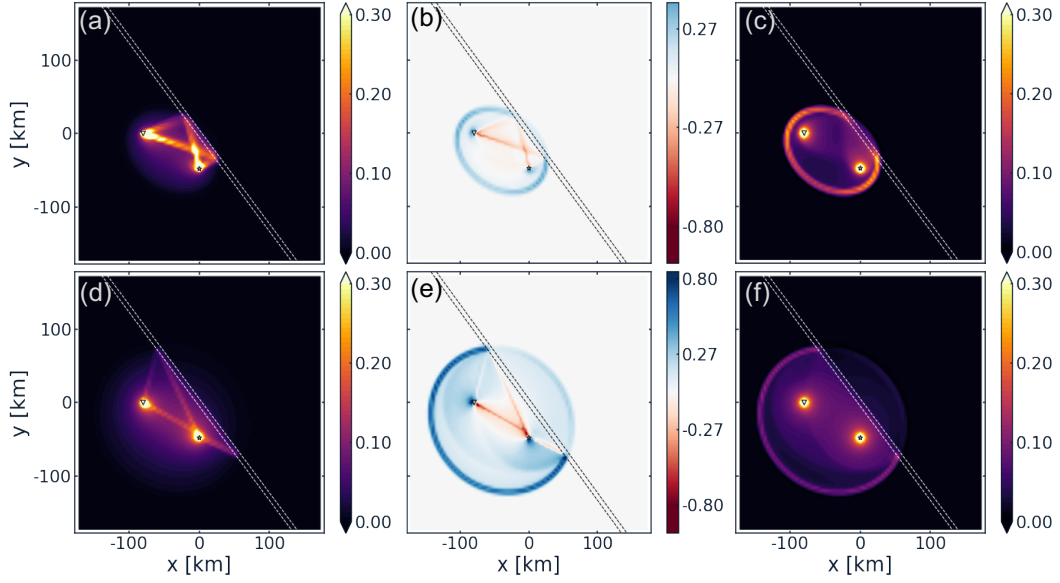


Figure 11. Sensitivity kernels for fault zone setting with both sources on one side of the fault (dashed lines), for lapse-times of 65 s (upper) and 100 s (lower). The columns show K_{tt} , K_{sc} and K_{dc} , respectively. The width of the fault zone is 6.25 km. The scattering mean free path in and outside the fault zone are $\ell_{FZ} = 10$ km and $\ell = 150$ km, respectively. The distance between the two sources is approximately 93 km. All kernels are normalised with respect to the maximum value. The color bar for K_{sc} is symmetric around zero.

559 Note that due to the inter-source distance of ~ 93 km in combination with a seismic ve-
 560 locity of 2.1 km s^{-1} , the earliest lapse-times for which the kernels are evaluated are around
 561 45 s. The travel-time and scattering kernels may appear more complex than kernels shown
 562 for the other non-uniform media. In the travel-time kernel we observe two additional two-
 563 legged transport paths that connect the source and the detector. They are actually gen-
 564 erated at the intersections of the single scattering ellipse with the fault zone where the
 565 strong scattering acts as secondary sources. For each of these paths, the backward and
 566 forward intensities are in exactly opposite directions. As explained for the K_{tt} of other
 567 models, the overlap of the specific intensities of either primary and/or secondary sources
 568 (in opposite direction) causes high sensitivities in the travel-time kernels. For the fault
 569 zone setting, this results in multiple pathways that are favorable for energy transport
 570 between the two primary sources (Fig. 11 a & d). For early lapse-time (65 s) we can ob-
 571 serve a spot with even higher concentrated sensitivity, at the intersection of the energy
 572 transport paths. Furthermore, the geometry of these additional paths between the pri-
 573 mary sources changes with lapse-time, as can be more clearly observed in the animations
 574 in the supporting information (Movie S4).

575 Fig. 11 (b & e) show similar observations for the scattering kernel, where the si-
 576 multaneously large and aligned energy fluxes create additional energy transport paths
 577 between the primary sources in the scattering kernel. The contribution of the high mean
 578 intensities is also visible in K_{sc} , which is similar to the halos of high sensitivities that
 579 are formed around the sources in the decorrelation kernel. Again K_{dc} does not resem-
 580 ble K_{tt} , and shows that the highly diffusive fault zone acts as a barrier for energy pass-
 581 ing through. Hence, the mean intensity is low on the right side of the fault zone in Fig.
 582 11 (f). In the supporting information, additional animations for K_{sc} (Movie S5) and K_{dc}
 583 (Movie S6) with lapse-time for the fault zone setting can be found.

584 **5 Concluding Remarks**

585 For monitoring the temporal evolution of the subsurface we need coda wave sen-
 586 sitivity kernels that linearly relate observed changes in recordings to physical medium
 587 changes. Here we compute travel-time, scattering and decorrelation kernels based on a
 588 flexible Monte Carlo method, which enables us to include non-uniformly distributed scat-
 589 tering properties. In this work we have shown that non-uniform scattering properties can
 590 have a profound and non-intuitive effect on coda wave sensitivity kernels. Hence, it could

591 be misleading to overlook the distribution of scattering properties in monitoring appli-
 592 cations. The actual impact on the kernels depends on a combination of lapse-time and
 593 mean free time, it is therefore important to have knowledge about the geology and an
 594 estimate on the scattering mean free path in the wider region that is targeted to be mon-
 595 itored.

596 There are two unique energy sources considered in the kernel computation for ei-
 597 ther uniform or non-uniform cases, namely the one from the source and the one from the
 598 detector, also referred to as the source of forward intensity and of backward intensity,
 599 respectively. Yet we have shown that due to non-uniform scattering properties additional
 600 energy transport channels can appear between the two sources, which do not exist in the
 601 case of a uniform scattering medium. Therefore, the sensitivity kernels for non-uniform
 602 scattering media can appear rather complex. The physical interpretation of the three
 603 different kernels is as follows: (1) the decorrelation kernel is the most straightforward
 604 to interpret and has high sensitivities where the mean intensities are high; (2) the travel-
 605 time kernel requires that the forward and backward specific intensities are simultane-
 606 ously large and in opposite direction; (3) the scattering kernel combines the properties
 607 of both the decorrelation and travel-time kernel and has high absolute sensitivities where
 608 the energy fluxes are simultaneously large and parallel or anti-parallel. Furthermore, the
 609 pattern of positive and negative sensitivities in the scattering kernel is controlled by the
 610 scalar product of the current fluxes from the forward and backward sources. The inter-
 611 pretation of the scattering kernel is more intuitive when considering the dominant con-
 612 tributions to the energy fluxes.

613 There are two types of fluxes contributing to the resulting fluxes around the two
 614 sources: (1) the direct flux between the forward and backward sources, and (2) the flux
 615 induced by the non-uniformity of scattering strength. The direction and magnitude of
 616 these two fluxes in turn depend on several parameters including distance from the bound-
 617 ary of scattering contrast, inter-source distance, orientation of the sources w.r.t. each
 618 other and the scattering contrast. In order to fully understand the scattering kernels,
 619 it requires knowledge of these actual fluxes, primarily from the sources and secondar-
 620 ily governed by the distribution of scattering, because the magnitude and direction of
 621 the fluxes may lead to additional pathways for energy transport between the two unique
 622 sources. Regarding Eq. (12), the interpretation of the energy propagation as energy fluxes
 623 is only valid in the diffusion regime. Yet with our findings it appears that this interpre-

624 tation may be extended to any propagation regime. However, more rigorous mathemat-
625 ical work is required to prove this.

626 Finally, this study visually demonstrates the difference between travel-time and decor-
627 relation kernels, although mathematically this has already been shown by Margerin et
628 al. (2016). Therefore, it emphasises that one needs to be careful with uncontrolled ap-
629 proximations. In our context, generic formulas derived in the diffusion regime cannot be
630 extended to the ballistic regime by simply substituting the heat diffusion Green’s func-
631 tion with a more accurate Green’s function derived from radiative transport theory. The
632 key issue is that diffusion theory does not allow to distinguish between decorrelation and
633 travel-time kernels because it relies on average intensities. This deficiency cannot be fixed
634 a-posteriori.

635 **Acknowledgments**

636 We acknowledge the support from the European Research Council (ERC) under the Eu-
637 ropean Union’s Horizon 2020 research and innovation program (grant agreement No 742335,
638 F-IMAGE). This work was granted access to the HPC resources of CALMIP supercom-
639 puting center under the allocation 2020-p19038, where the majority of the simulations
640 have been run. Some of the computations presented in this paper were performed us-
641 ing the CIMENT infrastructure (<https://ciment.ujf-grenoble.fr>), which is supported by
642 the Rhône-Alpes region (grant CPER07_13 CIRA: (<http://www.ci-ra.org>) and France-
643 Grille (<http://www.france-grilles.fr>)). The code used for the numerical simulations is cur-
644 rently being archived and will be made publicly available on <https://doc.archives-ouvertes.fr/en/>.

645 **References**

- 646 Arridge, S. R. (1995). Photon-measurement density functions. part I: Analytical
647 forms. *Applied Optics*, *34*(31), 7395–7409.
- 648 Barajas, A. (2021). *Imaging for scattering properties of the crust: body to surface*
649 *waves coupling* (Unpublished doctoral dissertation).
- 650 Brenguier, F., Campillo, M., Hadziioannou, C., Shapiro, N. M., Nadeau, R. M., &
651 Larose, E. (2008). Postseismic relaxation along the San Andreas fault at
652 Parkfield from continuous seismological observations. *science*, *321*(5895),
653 1478–1481.
- 654 Brenguier, F., Rivet, D., Obermann, A., Nakata, N., Boué, P., Lecocq, T., . . .

- 655 Shapiro, N. (2016). 4-D noise-based seismology at volcanoes: Ongoing ef-
656 forts and perspectives. *Journal of Volcanology and Geothermal Research*, *321*,
657 182–195.
- 658 Chen, J. H., Froment, B., Liu, Q. Y., & Campillo, M. (2010). Distribution of seis-
659 mic wave speed changes associated with the 12 may 2008 mw 7.9 wenchuan
660 earthquake. *Geophysical Research Letters*, *37*(18).
- 661 Duran, A., Planès, T., & Obermann, A. (2020). Coda-wave decorrelation sensitivity
662 kernels in 2-d elastic media: a numerical approach. *Geophysical Journal Inter-
663 national*, *223*(2), 934–943.
- 664 Gaebler, P., Eken, T., Bektaş, H. Ö., Eulenfeld, T., Wegler, U., & Taymaz, T.
665 (2019). Imaging of shear wave attenuation along the central part of the North
666 Anatolian Fault Zone, Turkey. *Journal of Seismology*, *23*(4), 913–927.
- 667 Hillers, G., Husen, S., Obermann, A., Planès, T., Larose, E., & Campillo, M. (2015).
668 Noise-based monitoring and imaging of aseismic transient deformation induced
669 by the 2006 Basel reservoir stimulation. *Geophysics*, *80*(4), KS51–KS68.
- 670 Hillers, G., T. Vuorinen, T. A., Uski, M. R., Kortström, J. T., Mäntyniemi, P. B.,
671 Tiira, T., ... Saarno, T. (2020). The 2018 geothermal reservoir stimula-
672 tion in Espoo/Helsinki, southern Finland: Seismic network anatomy and data
673 features. *Seismological Research Letters*, *91*(2A), 770–786.
- 674 Hirose, T., Nakahara, H., & Nishimura, T. (2017). Combined use of repeated ac-
675 tive shots and ambient noise to detect temporal changes in seismic velocity:
676 Application to Sakurajima volcano, Japan. *Earth, Planets and Space*, *69*(1),
677 42.
- 678 Hirose, T., Nakahara, H., & Nishimura, T. (2019). A passive estimation method
679 of scattering and intrinsic absorption parameters from envelopes of seismic
680 ambient noise cross-correlation functions. *Geophysical Research Letters*, *46*(7),
681 3634–3642.
- 682 Hoshiaba, M. (1991). Simulation of multiple-scattered coda wave excitation based
683 on the energy conservation law. *Physics of the Earth and Planetary Interiors*,
684 *67*(1-2), 123–136.
- 685 Kanu, C., & Snieder, R. (2015a). Numerical computation of the sensitivity kernel for
686 monitoring weak changes with multiply scattered acoustic waves. *Geophysical
687 Supplements to the Monthly Notices of the Royal Astronomical Society*, *203*(3),

- 688 1923–1936.
- 689 Kanu, C., & Snieder, R. (2015b). Time-lapse imaging of a localized weak change
690 with multiply scattered waves using numerical-based sensitivity kernel. *Journal*
691 *of Geophysical Research: Solid Earth*, *120*(8), 5595–5605.
- 692 Lux, I., & Koblinger, L. (1991). *Monte Carlo particle transport methods: neutron*
693 *and photon calculations*. CRC Press.
- 694 Mao, S., Campillo, M., van der Hilst, R. D., Brenguier, F., Stehly, L., & Hillers, G.
695 (2019). High temporal resolution monitoring of small variations in crustal
696 strain by dense seismic arrays. *Geophysical Research Letters*, *46*(1), 128–137.
- 697 Margerin, L. (2005). Introduction to radiative transfer of seismic waves. *Geophysical*
698 *Monograph-American Geophysical Union*, *157*, 229.
- 699 Margerin, L., Bajaras, A., & Campillo, M. (2019). A scalar radiative transfer model
700 including the coupling between surface and body waves. *Geophysical Journal*
701 *International*, *219*(2), 1092–1108.
- 702 Margerin, L., Campillo, M., & Van Tiggelen, B. (2000). Monte Carlo simulation
703 of multiple scattering of elastic waves. *Journal of Geophysical Research: Solid*
704 *Earth*, *105*(B4), 7873–7892.
- 705 Margerin, L., Planès, T., Mayor, J., & Calvet, M. (2016). Sensitivity kernels for
706 coda-wave interferometry and scattering tomography: theory and numerical
707 evaluation in two-dimensional anisotropically scattering media. *Geophysical*
708 *Journal International*, *204*(1), 650–666.
- 709 Mayor, J., Margerin, L., & Calvet, M. (2014). Sensitivity of coda waves to spa-
710 tial variations of absorption and scattering: radiative transfer theory and 2-D
711 examples. *Geophysical Journal International*, *197*(2), 1117–1137.
- 712 Mordret, A., Jolly, A., Duputel, Z., & Fournier, N. (2010). Monitoring of phreatic
713 eruptions using interferometry on retrieved cross-correlation function from
714 ambient seismic noise: Results from Mt. Ruapehu, New Zealand. *Journal of*
715 *Volcanology and Geothermal Research*, *191*(1-2), 46–59.
- 716 Obermann, A., Kraft, T., Larose, E., & Wiemer, S. (2015). Potential of ambient
717 seismic noise techniques to monitor the St. Gallen geothermal site (Switzer-
718 land). *Journal of Geophysical Research: Solid Earth*, *120*(6), 4301–4316.
- 719 Obermann, A., Planès, T., Hadziioannou, C., & Campillo, M. (2016). Lapse-time-
720 dependent coda-wave depth sensitivity to local velocity perturbations in 3-D

- 721 heterogeneous elastic media. *Geophysical Journal International*, 207(1), 59–
722 66.
- 723 Obermann, A., Planes, T., Larose, E., & Campillo, M. (2013). Imaging preruptive
724 and coeruptive structural and mechanical changes of a volcano with ambient
725 seismic noise. *Journal of Geophysical Research: Solid Earth*, 118(12), 6285–
726 6294.
- 727 Obermann, A., Planes, T., Larose, E., & Campillo, M. (2019). 4-D imaging of
728 subsurface changes with coda waves: Numerical studies of 3-D combined sen-
729 sitivity kernels and applications to the m_w 7.9, 2008 Wenchuan earthquake.
730 *Pure and Applied Geophysics*, 176(3), 1243–1254.
- 731 Obermann, A., Planès, T., Larose, E., Sens-Schönfelder, C., & Campillo, M. (2013).
732 Depth sensitivity of seismic coda waves to velocity perturbations in an elastic
733 heterogeneous medium. *Geophysical Journal International*, 194(1), 372–382.
- 734 Ogiso, M. (2019). A method for mapping intrinsic attenuation factors and scattering
735 coefficients of s waves in 3-d space and its application in southwestern japan.
736 *Geophysical Journal International*, 216(2), 948–957.
- 737 Paasschens, J. (1997). Solution of the time-dependent Boltzmann equation. *Physical*
738 *Review E*, 56(1), 1135.
- 739 Pacheco, C., & Snieder, R. (2005). Time-lapse travel time change of multiply
740 scattered acoustic waves. *The Journal of the Acoustical Society of America*,
741 118(3), 1300–1310.
- 742 Pacheco, C., & Snieder, R. (2006). Time-lapse travelttime change of singly scattered
743 acoustic waves. *Geophysical Journal International*, 165(2), 485–500.
- 744 Peng, Z., & Ben-Zion, Y. (2006). Temporal changes of shallow seismic velocity
745 around the Karadere-düzce branch of the north Anatolian fault and strong
746 ground motion. *Pure and Applied Geophysics*, 163(2-3), 567–600.
- 747 Planès, T., Larose, E., Margerin, L., Rossetto, V., & Sens-Schönfelder, C. (2014).
748 Decorrelation and phase-shift of coda waves induced by local changes: multiple
749 scattering approach and numerical validation. *Waves in Random and Complex*
750 *Media*, 24(2), 99–125.
- 751 Poupinet, G., Ellsworth, W., & Frechet, J. (1984). Monitoring velocity variations
752 in the crust using earthquake doublets: An application to the Calaveras Fault,
753 California. *Journal of Geophysical Research: Solid Earth*, 89(B7), 5719–5731.

- 754 Rivet, D., Campillo, M., Radiguet, M., Zigone, D., Cruz-Atienza, V., Shapiro, N. M.,
 755 ... others (2014). Seismic velocity changes, strain rate and non-volcanic
 756 tremors during the 2009–2010 slow slip event in Guerrero, Mexico. *Geophysical*
 757 *Journal International*, 196(1), 447–460.
- 758 Roux, P., & Ben-Zion, Y. (2014). Monitoring fault zone environments with cor-
 759 relations of earthquake waveforms. *Geophysical Journal International*, 196(2),
 760 1073–1081.
- 761 Sánchez-Pastor, P., Obermann, A., & Schimmel, M. (2018). Detecting and locat-
 762 ing precursory signals during the 2011 El Hierro, Canary Islands, submarine
 763 eruption. *Geophysical Research Letters*, 45(19), 10–288.
- 764 Sato, H. (1993). Energy transportation in one-and two-dimensional scattering media:
 765 analytic solutions of the multiple isotropic scattering model. *Geophysical Jour-*
 766 *nal International*, 112(1), 141–146.
- 767 Schaff, D. P., & Beroza, G. C. (2004). Coseismic and postseismic velocity changes
 768 measured by repeating earthquakes. *Journal of Geophysical Research: Solid*
 769 *Earth*, 109(B10).
- 770 Sens-Schönfelder, C., Bataille, K., & Bianchi, M. (2020). High frequency (6 hz)
 771 pkpab precursors and their sensitivity to deep earth heterogeneity. *Geophysical*
 772 *Research Letters*, e2020GL089203.
- 773 Sens-Schönfelder, C., & Wegler, U. (2006). Passive image interferometry and sea-
 774 sonal variations of seismic velocities at Merapi Volcano, Indonesia. *Geophysical*
 775 *research letters*, 33(21).
- 776 Shearer, P. M., & Earle, P. S. (2004). The global short-period wavefield modelled
 777 with a Monte Carlo seismic phonon method. *Geophysical Journal Interna-*
 778 *tional*, 158(3), 1103–1117.
- 779 Snieder, R., Duran, A., & Obermann, A. (2019). Locating velocity changes in elastic
 780 media with coda wave interferometry. *Seismic Ambient Noise*, 188.
- 781 Snieder, R., Grêt, A., Douma, H., & Scales, J. (2002). Coda wave interferome-
 782 try for estimating nonlinear behavior in seismic velocity. *Science*, 295(5563),
 783 2253–2255.
- 784 Takeuchi, N. (2016). Differential monte carlo method for computing seismogram
 785 envelopes and their partial derivatives. *Journal of Geophysical Research: Solid*
 786 *Earth*, 121(5), 3428–3444.

- 787 van Dinther, C., Margerin, L., & Campillo, M. (2020). Laterally varying scatter-
788 ing properties in the North Anatolian Fault Zone from ambient noise cross-
789 correlations. *Geophysical Journal International*.
- 790 Wegler, U., & Lühr, B. G. (2001). Scattering behaviour at merapi volcano (java)
791 revealed from an active seismic experiment. *Geophysical Journal International*,
792 *145*(3), 579–592.
- 793 Wilson, B. C., & Adam, G. (1983). A Monte Carlo model for the absorption and
794 flux distributions of light in tissue. *Medical physics*, *10*(6), 824–830.
- 795 Wu, C., Peng, Z., & Ben-Zion, Y. (2009). Non-linearity and temporal changes of
796 fault zone site response associated with strong ground motion. *Geophysical*
797 *Journal International*, *176*(1), 265–278.
- 798 Yamamoto, M., & Sato, H. (2010). Multiple scattering and mode conversion re-
799 vealed by an active seismic experiment at asama volcano, japan. *Journal of*
800 *Geophysical Research: Solid Earth*, *115*(B7).
- 801 Yoshimoto, K., Wegler, U., & Korn, M. (2006). A volcanic front as a boundary of
802 seismic-attenuation structures in northeastern Honshu, Japan. *Bulletin of the*
803 *Seismological Society of America*, *96*(2), 637–646.
- 804 Zhang, T., Sens-Schönfelder, C., & Margerin, L. (2021). Sensitivity kernels for
805 static and dynamic tomography of scattering and absorbing media with elastic
806 waves: a probabilistic approach. *Geophysical Journal International*.